RSC Advances

PAPER

View Article Online
View Journal | View Issue

Cite this: *RSC Adv.*, 2021, **11**, 15457

Release of methane from nanochannels through displacement using CO_2

Xu Cheng,[a] Zhigang Li*[a] and Ya-Ling He*[b]

Received 7th March 2021
Accepted 15th April 2021

DOI: 10.1039/d1ra01795k

rsc.li/rsc-advances

In this work, we investigate the release of methane in quartz nanochannels through the method of displacement using carbon dioxide. Molecular dynamics (MD) simulations and theoretical analysis are performed to obtain the release percentage of methane for nanochannels of various diameters. It is found that both the pressure of CO_2 and the channel size affect the release percentage of methane, which increases with increasing pressure of CO_2 and channel diameter. Without CO_2, the majority of methane molecules are adsorbed by the channel surface. When CO_2 is injected into the channel, CO_2 molecules replace many methane molecules due to the relatively strong molecular interactions between CO_2 and the channel, which leads to the desorption of methane, reduces the energy barrier for the transport of methane, and consequently increases the release rate. Theoretical predictions using the kinetic energy of methane and the energy barrier inside the channel are also conducted, which are in good agreement with the MD simulations.

1. Introduction

In the past decades, the rapid increase of energy consumption has posed a challenge to the growth of the worldwide economy, which has motivated the exploration of new energy sources. Among various alternatives, shale gas has become a promising source for solving the potential energy crisis.[1] Compared with the traditional fossil fuels, shale gas is eco-friendly due to its low carbon emission.[2,3] For the exploitation of shale gas, the combination of hydraulic fracturing and horizontal drilling is the most widely used technology for mass production.[4] However, this technology consumes a large amount of water and has potential contamination of underground water.[5–7] Moreover, the output of a typical shale gas well usually experiences a significant drop after three years.[8,9] Therefore, it is important to find new methods to exploit shale gas.

Shale gas mainly contains methane, which is trapped in nanoscale pores of shale.[10,11] The strong confinements of the nanopores make the release of shale gas a nontrivial process. In the literature, many efforts have been made to study the adsorption and desorption of methane molecules in nanopores through experiments and simulations. Rexer *et al.*[12] examined the adsorption of methane in shale samples through experiments by varying the temperature and pressure according to various geological conditions of shale gas. They measured and modeled the methane excess uptake and isosteric enthalpy, which provide useful information for understanding the storage mechanisms of shale gas. Lithoxoos *et al.*[13] numerically investigated the capacity of single-wall carbon nanotubes (SWCNTs) for methane storage at room temperature under different pressures and the results were confirmed by experiments. They obtained the density distributions of different gases and found that almost all the gas molecules were adsorbed by the interior surface of the pores. Zhu and Zhao[14] explored the mechanisms of methane adsorption in CNTs through molecular dynamics (MD) simulations and proposed an equation of state for the adsorbed phase of methane molecules. Their equation can predict most of the adsorption phenomena observed in their simulations. Furthermore, they found that the adsorption behavior in nanopores was affected by the size and curvature of the pores. As a consequence, there exists an optimal CNT diameter that maximizes the adsorption of methane. Wu *et al.*[15] also studied the mechanisms of methane adsorption and displacement processes in carbon nanochannels through MD simulations and obtained similar results to those of Zhu and Zhao.[14] It was found that when the external pressure reaches 5 MPa, the adsorption isotherms for bulk methane is about 1.5 mmol cm^{-3}, whereas it is about 10 mmol cm^{-3} in nanopores. Bartus *et al.*[16] studied the behavior of methane molecules inside rigid and flexible carbon nanotubes (CNTs) at room temperature through classical MD simulations and obtained that the diffusion coefficient in rigid and flexible CNTs are similar. Mahdizadeh *et al.*[17] used grand canonical Monte Carlo (GCMC) simulations to investigate the methane adsorption in single-walled carbon nanotubes (SWCNTs) and their results indicate that SWCNTs can be stylized for methane adsorption. Liu *et al.*[18] explored the diffusion of methane at room

---

[a] *Department of Mechanical and Aerospace Engineering, The Hong Kong University of Science and Technology, Clear Water Bay, Kowloon, Hong Kong. E-mail: mezli@ust.hk*

[b] *Key Laboratory of Thermo-Fluid Science and Engineering of MOE, School of Energy and Power Engineering, Xi'an Jiaotong University, Xi'an, Shaanxi 710049, PR China. E-mail: yalinghe@mail.xjtu.edu.cn*

temperature under various pressures in dry and wetted CNTs with different diameters through MD simulations. They reported that the diffusion coefficient of methane molecules reduces dramatically in wetted CNTs compared with that in dry CNTs because the low solubility of CH_4, especially in thin CNTs.

In addition, there are some studies comparing the adsorption of CH_4 and CO_2 in nanoconfinements. Huang *et al.*[19] used GCMC simulations to examine the adsorption behavior of an equimolar CO_2/CH_4 mixture in CNTs by considering the effects of pressure, temperature, and CNT diameter. They found that the adsorption of CO_2 is much stronger than that of CH_4 and the influences of temperature and pressure are minor in small CNTs and the CNT size affects the adsorption of CO_2 more significantly than that of CH_4. Lu *et al.*[20] compared the selectivity of several nanostructures for CO_2/CH_4 mixtures through GCMC simulations and found that CNTs have the highest selectivity. Liu *et al.*[21] reported a comparison of the adsorption of CO_2/CH_4 mixtures of three different types of carbon nanopores at different temperatures and observed that the selectivity of these carbon nanopores decreases with increasing temperature and the (7, 7) CNT has the highest selectivity of CO_2. Cao *et al.*[22] changed the hydrophilicity of CNTs by changing the number of –CO groups and found that the selectivity of CO_2 increases with increasing hydrophilicity. Moreover, Hong *et al.*[23] investigated the adsorption capacity of open-ended SWCNTs for various gases, especially CO, and found that under the conditions of room temperature and 1 atm, the (8, 8) open-ended SWCNT presents a high adsorption capacity for CO.

Another approach for developing shale gas is to replace it by other species. Some studies have been conducted to investigate the performance of this method. Yu *et al.*[24] built an experimental apparatus to obtain the transport characteristics of methane in nanopores and found that carbon dioxide is easier to be adsorbed by the pore surface than methane. Bhowmik *et al.*[25] investigated the displacement behavior of methane by pure carbon dioxide in dry, powdered, bituminous Indian coals. It was also found that carbon dioxide is preferentially adsorbed by silt pores compared with methane. However, most of the previous experimental work is mainly focused on macroscopic studies. Only a few studies have been performed to understand the replacement of methane in nanopores perhaps because nanoscale studies are experimentally challenging. Huo *et al.*[26] collected 4 shale samples in Jiaoshiba area of Sichuan basin, China and investigated the displacement behavior of methane by carbon dioxide. It was found that the injection pressure of

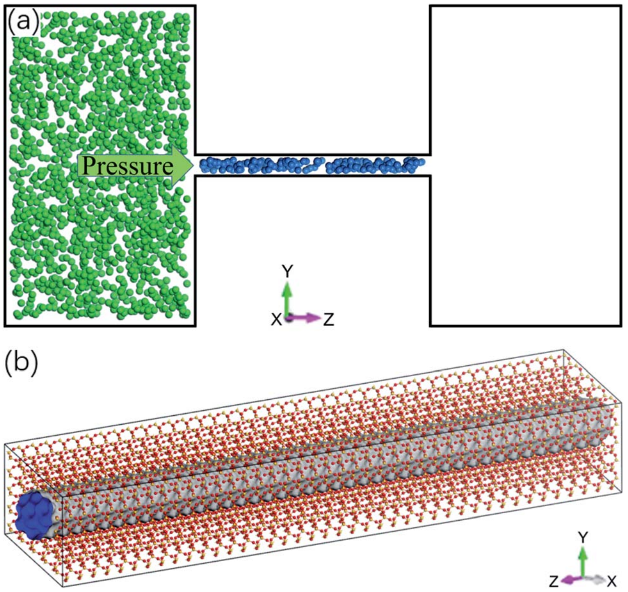

Fig. 1 Molecular dynamics simulation system. (a) Schematic of the system: a quartz nanochannel with two reservoirs at the ends (blue and green spheres are methane and CO_2 molecules). (b) Atomic structure of quartz nanochannel.

Table 1 Potential parameters for the force field

Bond stretch parameters

Bond type	K_0 (kcal mol^{-1} Å^{-2})	R_0 (Å)
C–H	700	1.09
Si–O	700	1.587
C–O	1400	1.152

Bond angle bend parameters

Bond type	K_0 (kcal mol^{-1} Å^{-2})	θ_0
H–C–H	100	109.471°
Si–O–Si	100	104.51°
O–Si–O	100	109.471°
O–C–O	100	180

Torsional parameters

Torsion type	B_0 (kcal mol^{-1})	d_0	n_0
O–Si–O–Si	2	−1	3

Lennard-Jones parameters

Interaction type	σ (Å)	ε (kcal mol^{-1})
H–H	3.195	0.015
C–C	3.898	0.095
H–C	3.547	0.038
H–O	3.3	0.038
H–Si	3.733	0.069
C–O	3.651	0.095
C–Si	4.084	0.172
O–O	3.405	0.096
O–Si	3.838	0.173

Electrostatic parameters

Element type	Charge (e)
C in methane	−0.4
C in carbon dioxide	0.572
H	0.1
O in carbon dioxide	−0.286
O in quartz	−0.445
Si	0.89

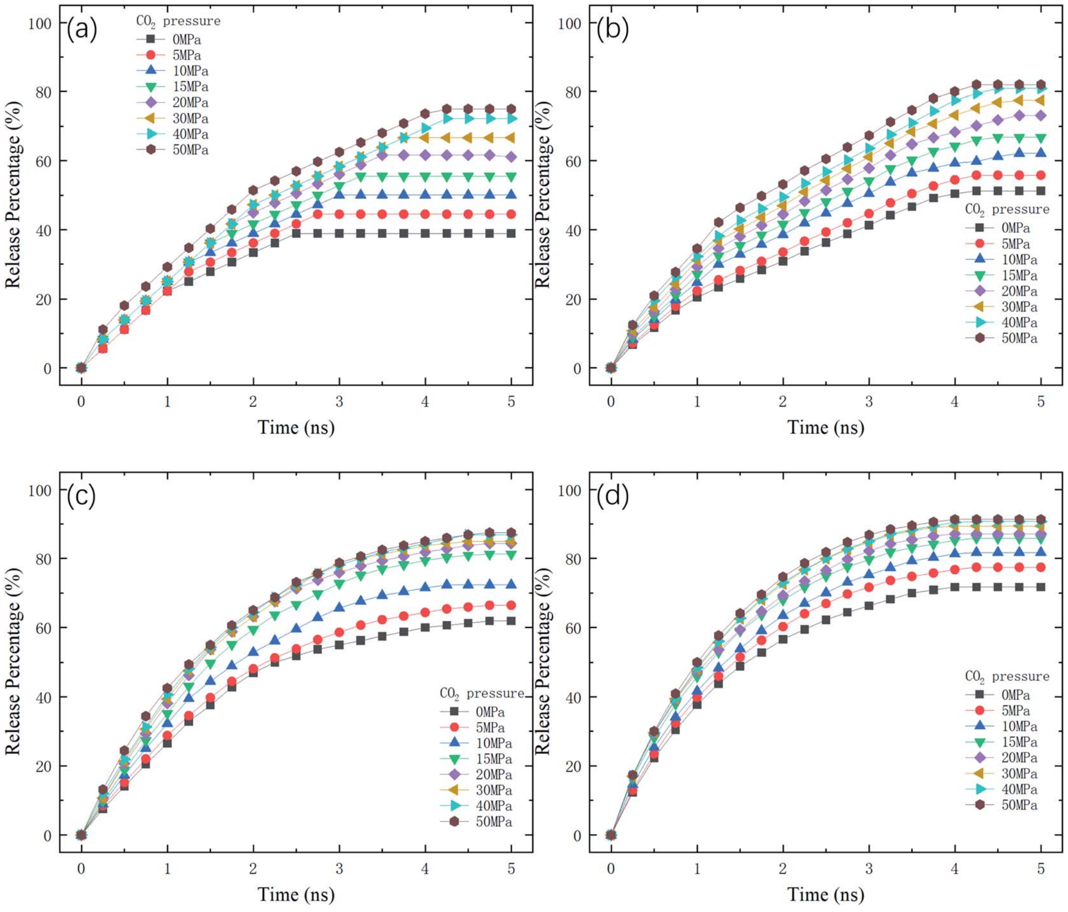

Fig. 2 Release percentage of methane as a function of time at different CO$_2$ pressures in channels with various diameters D. (a) $D = 1$ nm. (b) $D = 1.5$ nm. (c) $D = 2$ nm. (d) $D = 2.5$ nm.

carbon dioxide strongly affects the displacement process. The release rate of methane increases with increasing injection pressure of carbon dioxide. Their investigations provide preliminary knowledge for carbon dioxide sequestration in shale reservoirs.

As an alternative approach, numerical simulations have been conducted to probe the replacement process of shale gas in nanopores. Shi *et al.*[27] proposed a shale model using organic–inorganic composites and used Grand Canonical Monte Carlo (GCMC) and MD simulations to study the dynamics of methane driven by carbon dioxide. It was found that the amount of methane in the shale decreases dramatically as the injection pressure of carbon dioxide rises from 0 to 30 MPa. However, when the pressure of carbon dioxide is higher than 30 MPa, there is no further increase in the release rate of methane due to the CO$_2$ saturation in the pores. Zhang *et al.*[28] employed GCMC simulations to study the displacement of shale gas at different geological depths up to 4 km, they varied the geological conditions by changing the pressure and temperature of the system. The results indicate that carbon dioxide can displace methane molecules efficiently under the geological depth of 1 km. However, the displacement amount of methane decreases significantly when the geological depth is further increased. Sun *et al.*[29] investigated the microscopic adsorption and diffusion of methane and carbon dioxide in kerogen shale pores and studied the replacement of methane by carbon dioxide through MD simulations. It was revealed that methane can be replaced

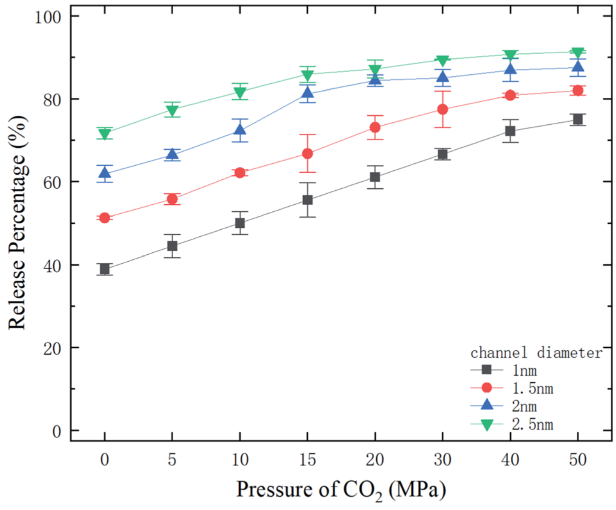

Fig. 3 The final release percentages of methane as a function of CO$_2$ pressure.

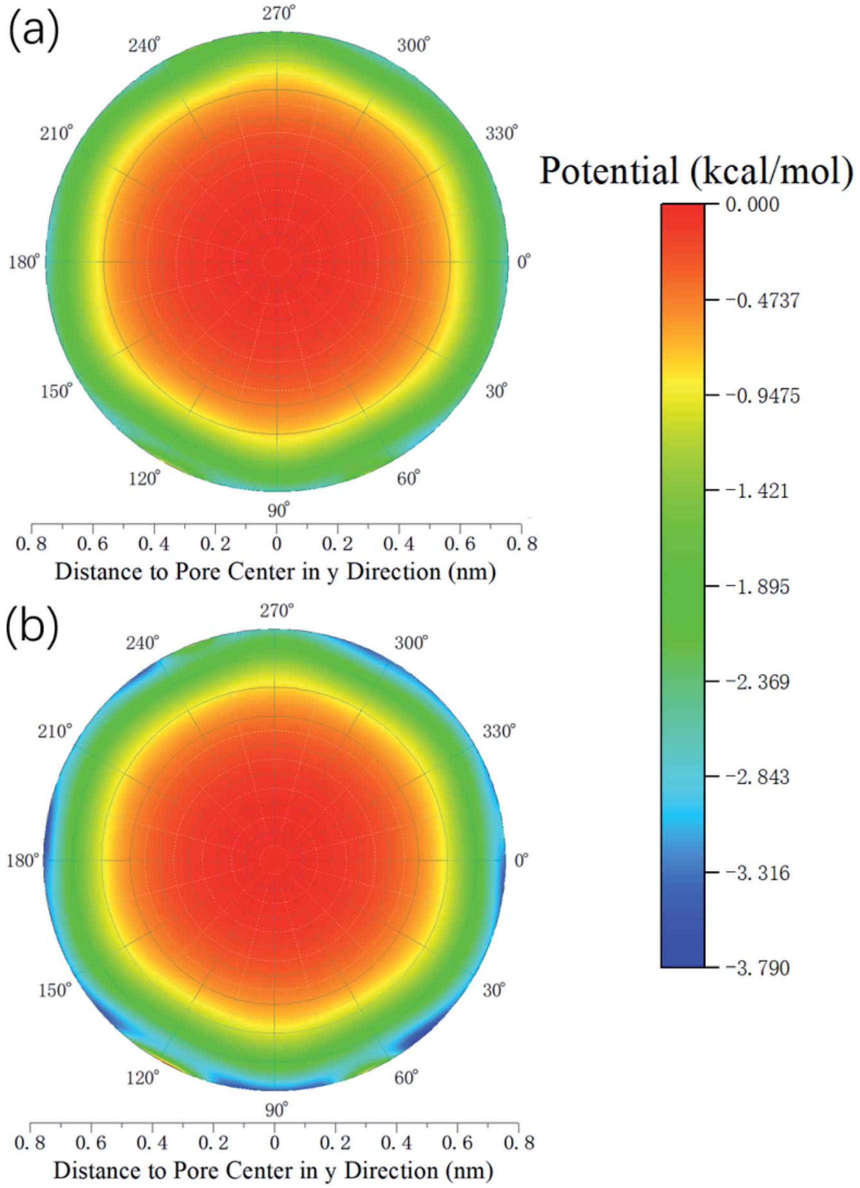

Fig. 4 Potential distribution inside the 2 nm-diameter channel in a plane perpendicular to the channel axis. (a) Methane (b) CO_2.

by carbon dioxide because carbon dioxide has stronger interaction with pore walls than methane. It was also observed that a small portion of methane molecules were hard to be replaced through carbon dioxide injection. Ho *et al.*[30] probed the release of CH_4 and CO_2 in kerogen and CNTs through MD simulations. It was found that the diffusion coefficient of CH_4 is higher than that of CO_2, which indicates that CO_2 is more difficult to be released from kerogen and CNTs that CH_4. Moreover, the impacts of water on the release of methane with and without the presence of CO_2 were also explored. Due to the relatively high solubility, CO_2 can be preferentially adsorbed in kerogen, leading to the release of methane. Yuan *et al.*[31] investigated the enhanced recovery of confined CH_4 with CO_2 by MD simulations and found that there exists an optimal CNT size for CH_4 displacement. Yang *et al.*[32] studied the adsorption and diffusion properties of CH_4 and CO_2 in CNTs with preabsorbed water at room temperature with different pressures. They found that the presence of water enhances the adsorption of CO_2 due to the CO_2–H_2O interaction and the adsorption selectivity of CO_2/CH_4 increases with increasing pressure. Although the displacement phenomena of methane has been observed in experiments and simulations, the microscopic mechanism of shale gas replacement in nanopores is still unclear, which requires extensive investigations.

In this work, we investigate the displacement of methane by carbon dioxide through MD simulations. The methane release percentage is obtained at various carbon dioxide injection pressures for different pore diameters. Quartz nanochannels with tetrahedral structure, which have been widely used for gas storage,[33,34] are employed to model shale pores. It is found that the release percentage of methane rises as the injection pressure of carbon dioxide is increased due to the relatively strong molecular interactions between carbon dioxide and channel walls. Furthermore, the release percentage of methane is theoretically predicted using the kinetic energy of methane molecules and the energy barrier inside the channel, which is in good agreement with MD simulations.

2. Molecular dynamics simulation

Molecular dynamics simulations are conducted using Material Studio. The simulation system contains a cylindrical quartz (silicon dioxide) nanochannel with two reservoirs at the ends, as illustrated in Fig. 1a. The structure of the channel is tetrahedral (Fig. 1b) and the diameter of the nanochannel ranges from 1 to 2.5 nm. The length of the nanochannel is 20 nm and the lengths of the two reservoirs are 15 nm, 25 nm, and 10 nm in the x, y, and z directions, respectively. The Berendsen thermostat and Parrinello–Rahman barostat are used to control the temperature and pressure of the system at 350 K and 20 MPa, which are similar to the real geological conditions of shale gas reservoirs.[35–37] Under these conditions, the density of methane is 119.41 kg m^{-3},[38] which is used to initially store methane molecules in the nanochannel. The left reservoir is filled with a certain number of CO_2 molecules, ranging from 4600 to 45 400, which generates a pressure in the reservoir from 5 to 50 MPa.[39] A special case without CO_2 injection is also studied, for which, there are no CO_2 molecules in the reservoir.

The DREIDING force field[40] is employed to describe the quartz channel, methane, and methane–channel interactions. The general potential for these interactions is given by

$$\begin{aligned} U = {} & \sum_{\text{bonds}} \frac{K_\text{b}}{2}(r_{ij}-R_0)^2 + \sum_{\text{angles}} \frac{K_\text{a}}{2}(\theta-\theta_0)^2 \\ & + \sum_{\text{torsions}} \frac{B_0}{2}(1-d_0\cos(n_0\phi)) \\ & + \sum_{i<j} 4\varepsilon_{ij}\left(\left(\frac{\sigma_{ij}}{r_{ij}}\right)^{12} - \left(\frac{\sigma_{ij}}{r_{ij}}\right)^{6}\right) + \sum_{i<j}\frac{q_iq_j}{r_{ij}} \end{aligned} \tag{1}$$

where K_0 is a force constant, R_0 and θ_0 are the equilibrium bond distance and angle, B_0 is the barrier height, d_0 is the phase

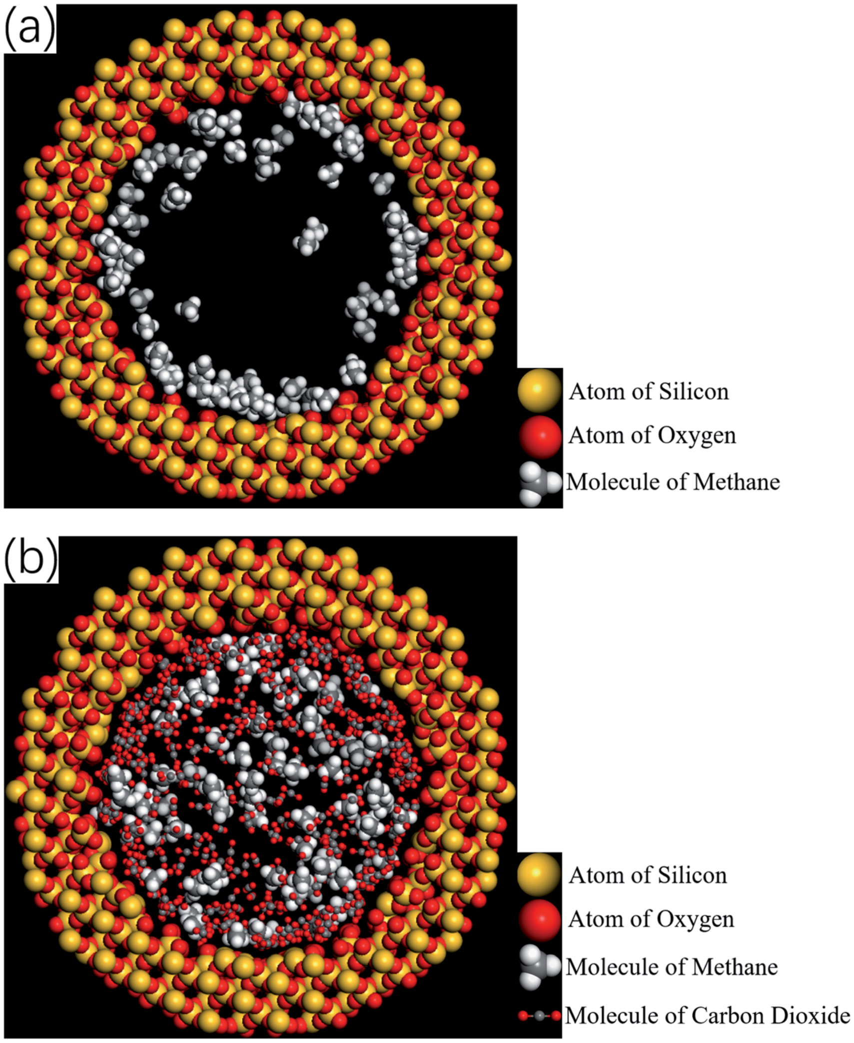

Fig. 5 Snapshots of simulations showing the spatial distributions of methane and CO_2 molecules. (a) Before the injection of CO_2 (the majority of methane molecules are adsorbed by the channel wall). (b) After the injection of CO_2 (some adsorbed methane molecules are replaced by CO_2 molecules and driven into the inner area of the channel).

factor, n_0 is the periodicity, ε is the binding energy and σ is the collision diameter, r_{ij} is the separation between molecules/atoms i and j, θ is the bond angle, ϕ is the bond torsion angle, and q is the charge. The values of relevant parameters for various interactions are listed in Table 1, where the bond stretch, bond angle bend, torsional, and Lennard-Jones parameters are adopted from the original DREIDING potential.[40] However, the charges for the electrostatic potential are estimated using the Gasterier method,[41] which have been confirmed by previous work.[31,42]

The cut-off distance for the potential is set at 10.5 Å and the time step is 1 fs. Initially, the reservoirs and the nanochannel are not connected (they are separated by a wall) and the system is relaxed for 200 ps in the (N, V, T) ensemble. After the relaxation, the walls between the reservoirs and the nanochannel are removed so that CO_2 molecules can infiltrate into the channel. At the same time, the system is performed in the (N, V, E) ensemble to calculate the release percentage of methane molecules.

3. Results and discussion

By varying the pressure of CO_2 and the channel diameter, the number of methane molecules expelled from the channel is obtained and the release percentage of methane is computed as

$$P_\mathrm{r} = \frac{N}{N_0} \times 100\%, \tag{2}$$

where N is the number of methane molecules released from the channel, *i.e.*, the number of methane molecules in the reservoirs, and N_0 is the total number of methane molecules in the system. Fig. 2 shows the release percentage as a function of time for different channel diameters under various CO_2 pressures. It is seen that P_r approaches constant values in 5 ns regardless of the channel size and CO_2 pressure. The final release percentage is depicted in Fig. 3. It is found that P_r increases as the pressure of CO_2 is raised. At zero CO_2 pressure, *i.e.*, initially no CO_2 in the left reservoir, P_r is about 40% for 1 nm-diameter channel, while it is about 70% for 2.5 nm diameter channel. This is because the reservoirs initially are vacuum and the high methane pressure inside the channel drives some methane molecules into the reservoirs. For 1 and 1.5 nm-diameter channels, P_r increases and eventually reaches about 80% and 85%, respectively, as the pressure of CO_2 increases, which indicates that the method of displacement using CO_2 works well. In 2 nm and 2.5 nm diameter channels, as the storage capacity of the channels for methane is weak, even if there is no CO_2 injection, P_r is over 60%. With CO_2 injection, P_r reaches about 90% and 95%, which demonstrates that the method of displacement is still useful for relatively large diameters.

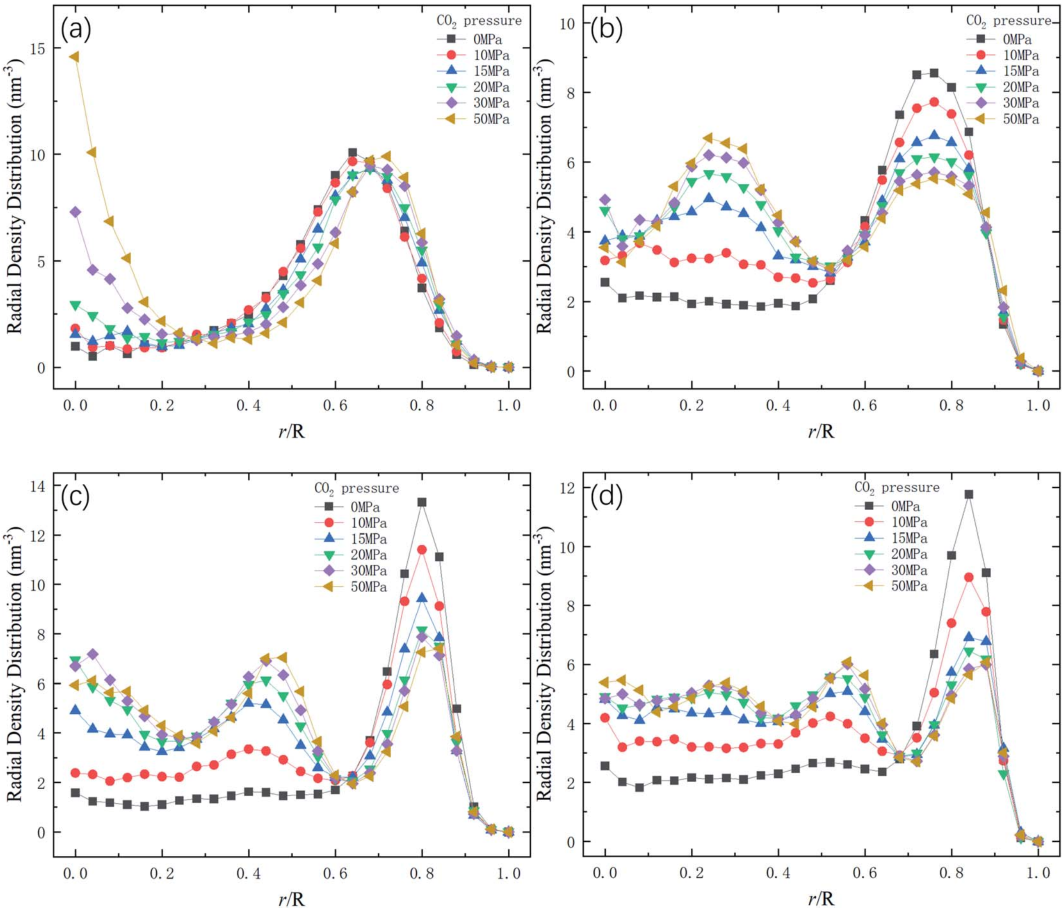

Fig. 6 Radial density distribution of methane in channels of different diameters D. R is the radius of the channel. (a) $D = 1$ nm. (b) $D = 1.5$ nm. (c) $D = 2$ nm. (d) $D = 2.5$ nm.

Whether a methane molecule can be released from the channel or not mainly depends on the kinetic energy E of the methane molecule and the energy barrier ΔG in the channel.[43–45] E is mainly determined by the temperature T and ΔG is governed by the methane–quartz molecular interaction and the pore structure. ΔG is the potential difference between the maximum and minimum potential points in the channel. If the kinetic energy of a methane molecule is sufficiently high, it can overcome the energy barrier and can be released from the channel. The probability for the methane molecules to escape from the attraction of the channel is proportional to $\exp(-\Delta G/E)$, as will be discussed later.

Therefore, the release percentage of methane can be enhanced by either increasing the kinetic energy E of methane molecules or reducing the energy barrier ΔG of the channel. In previous work,[46,47] we explored the method of increasing the kinetic energy E by heating or applying an external force on the channel to release methane from nanopores. Herein, by injecting CO_2, we expect to decrease the energy barrier ΔG in the channel through the displacement of methane molecules to increase the release percentage of methane. Fig. 4a and b show the potential distribution of methane and carbon dioxide, respectively, inside the 2 nm-diameter channel in a plane perpendicular to the channel axis. In Fig. 4a, it is seen that the potential energy of methane next to the wall is low and that at the center area is high. The low potential close to the wall is caused by strong methane–wall interactions, which lead to the adsorption of methane molecules on the channel surface, as demonstrated in Fig. 5a. As CO_2 molecules are injected into the channel, CO_2 molecules replace methane molecules on the adsorption sites of the channel wall because the CO_2–wall intermolecular interaction is stronger than that between methane and the wall, as indicated by the potential distribution in Fig. 4 (the potential energy of methane next to the wall is about 3 kcal mol^{-1} while that of carbon dioxide is about 3.8 kcal mol^{-1}). Consequently, some methane molecules are replaced by carbon dioxide molecules and freed from adsorption, as shown in Fig. 5b, which makes them easier to be released from the channel because the energy barrier to be overcome becomes smaller, as will be shown later. The replacement of methane molecules by CO_2 molecules can be manifested by the density distribution of methane in the channel as the pressure of CO_2 is varied, as depicted in Fig. 6. It is seen that the density of methane next to the wall decreases while the density around the center area increases as the CO_2 pressure is increased due to the adsorption of CO_2 on the channel surface and the replacement of methane by CO_2. Fig. 7 shows the density distribution of CO_2 in the channel. It is clear

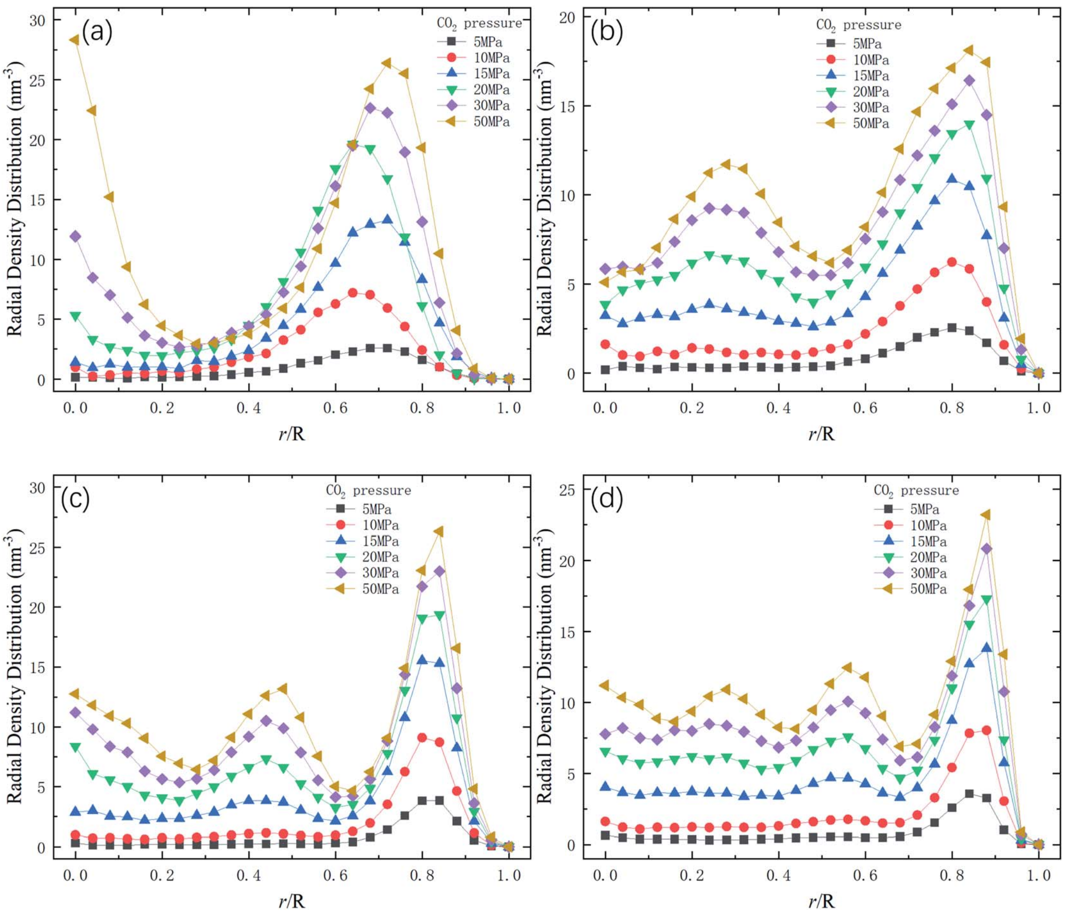

Fig. 7 Radial density distribution of carbon dioxide in channels of different diameters D. R is the radius of nanochannels. (a) $D = 1$ nm. (b) $D = 1.5$ nm. (c) $D = 2$ nm. (d) $D = 2.5$ nm.

that many CO_2 molecules are adsorbed by the channel surface and the adsorption is enhanced by the pressure. Fig. 7 confirms that CO_2 molecules can replace methane molecules efficiently. Fig. 8 shows the fraction of methane molecules as a function of potential energy in nanochannels. It is seen that the number of methane molecules with low potential energy decreases as the pressure of CO_2 is increased, which reduces the energy barrier for methane molecules, as will be shown later, and consequently increase the release percentage of methane.

As mentioned previously, the release percentage of methane molecules can be theoretically predicted using E and ΔG. Similar to the velocity, the kinetic energy of methane molecules follows the Maxwell–Boltzmann distribution,

$$f(E) = 2\sqrt{\frac{E}{\pi}}\left(\frac{1}{k_{\mathrm{B}}T}\right)^{3/2} \mathrm{e}^{\left(\frac{-E}{k_{\mathrm{B}}T}\right)}, \tag{3}$$

where k_B is the Boltzmann constant. If the potential energy barrier in the quartz nanochannels is denoted as ΔG, the release percentage can be theoretically predicted as

$$P^* = 1 - \int_0^{\Delta G} 2\sqrt{\frac{E}{\pi}}\left(\frac{1}{k_{\mathrm{B}}T}\right)^{3/2} \mathrm{e}^{\left(\frac{-E}{k_{\mathrm{B}}T}\right)} \mathrm{d}E \tag{4}$$

The results of eqn (4) is proportional to $\exp(-\Delta G/k_BT)$, *i.e.*, $P^* \propto \exp(-\Delta G/k_BT)$. As ΔG is governed by the potential distribution inside the channels, and the potential U depends on the nature of atoms and position of molecules in the channels, the average potential $U_{avg}(z)$ along the axis of the channels is employed to obtain ΔG. $U_{avg}(z)$ is calculated through

$$U_{\mathrm{avg}}(z) = \frac{\iint_s U(x,y,z)\mathrm{e}^{-\beta U(x,y,z)}\mathrm{d}s}{\iint_s \mathrm{e}^{-\beta U(x,y,z)}\mathrm{d}s}, \tag{5}$$

where s is the area of adsorption site of methane molecules (for the cases without CO_2 injection and at low CO_2 pressures, s is the an interior surface next to the channel; at high CO_2 injection pressures, s is the whole inner space of the channel, *i.e.*, $r/R = 0$–0.65, where R is the radius of channel) and $\beta = 1/k_BT$. ΔG is calculated as the potential difference between the point where $U_{avg}(z)$ is the highest and the point where $U_{avg}(z)$ is the minimum.

Fig. 9 shows the potential energy barrier ΔG for methane as a function of CO_2 pressure in different nanochannels. It is seen that ΔG in small-diameter channels is higher than that in large-diameter channels. This is why the release percentage in small channels is relatively low, as shown in Fig. 3. Furthermore, ΔG decreases with increasing CO_2 pressure due to the displacement of methane by CO_2. On the basis of the ΔG values in Fig. 9, the

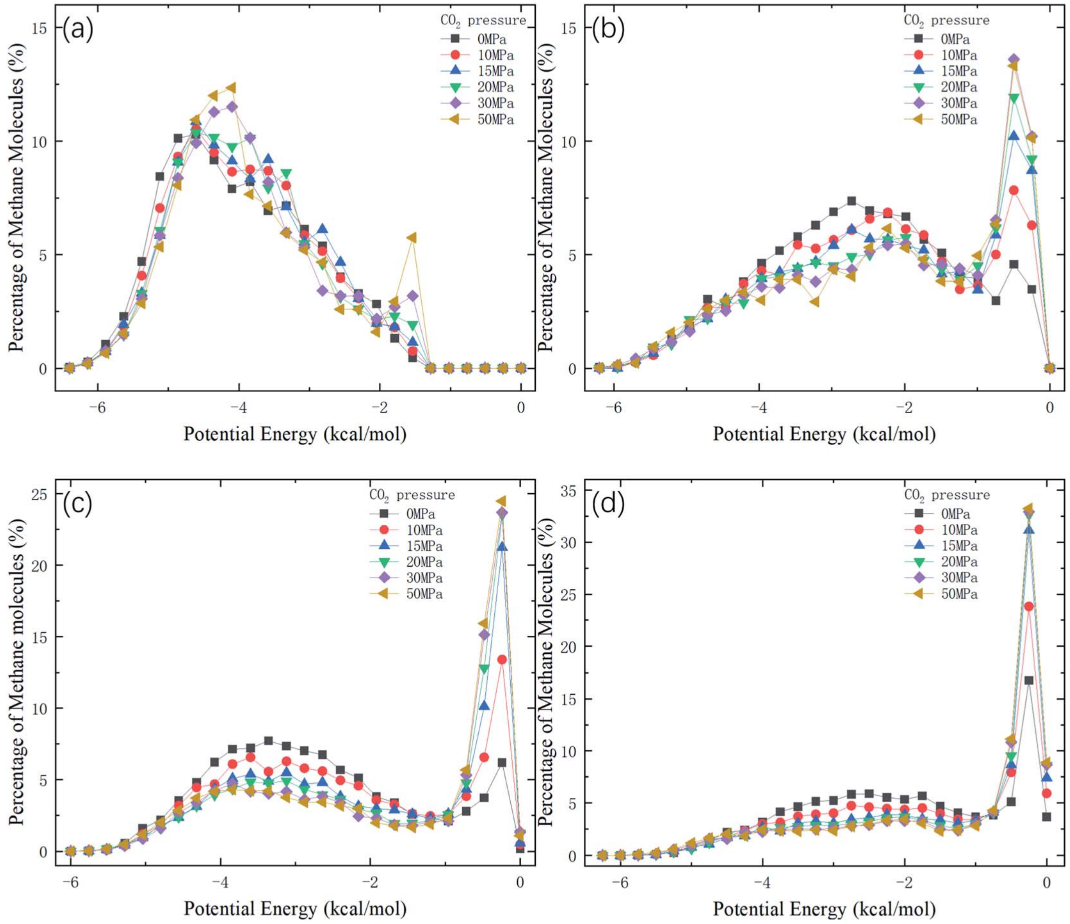

Fig. 8 Distribution of potential energy of methane in channels of different diameters D. (a) $D = 1$ nm. (b) $D = 1.5$ nm. (c) $D = 2$ nm. (d) $D = 2.5$ nm.

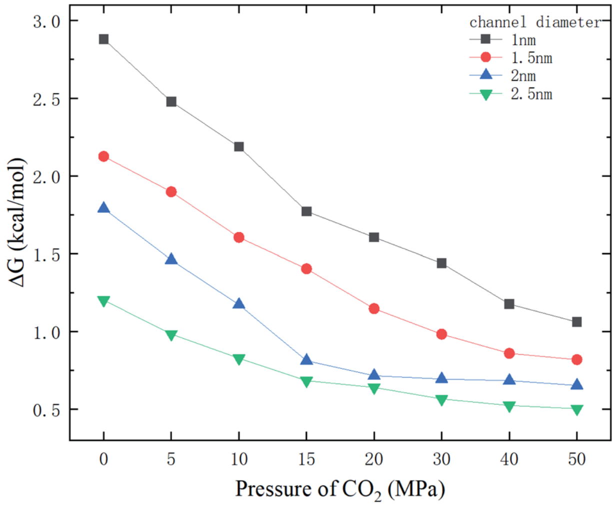

Fig. 9 Energy barrier ΔG as a function of CO_2 pressure.

release percentages predicted by eqn (4) are shown in Fig. 10. It is seen that the theoretical predictions are in good agreement with the MD results. The discrepancy is caused by the estimation of ΔG, which is obtained using the average potential in the channels.

With the ΔG data in Fig. 9, the variation of the release percentage in Fig. 3 can be explained. For a small-diameter nanochannel, when CO_2 is injected into the channel, CO_2 molecules occupy most of the space next to the channel wall and drive the methane molecules to the center area, which greatly reduces ΔG and increases the release percentage of methane (Fig. 3). In large nanochannels, ΔG is relatively small and is not sensitive to the CO_2 pressure (Fig. 8). This is why the release percentage of methane is high, even at low CO_2 pressures.

4. Conclusions

The displacement of methane molecules by carbon dioxide in nanochannels of different pore sizes has been studied through MD simulations. As the intermolecular interaction between carbon dioxide and the quartz nanochannel is stronger than the methane–channel interaction, some methane molecules are replaced by carbon dioxide molecules and expelled to the center area of the channel, where reduces the energy barrier for the transport of methane and consequently enhances the release percentage of methane. Theoretical predictions for the methane release percentage using the kinetic energy of methane and the energy barrier in the channel are also calculated, which are in good agreement with MD simulations.

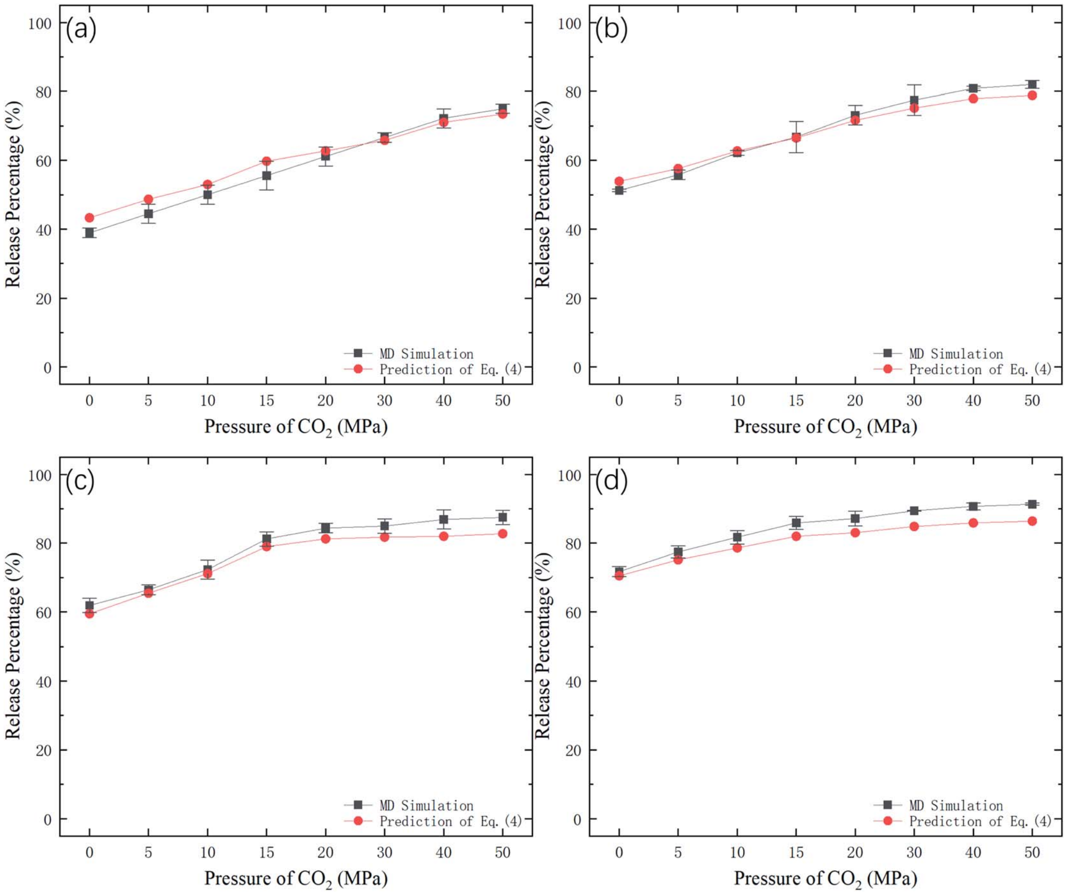

Fig. 10 Methane release percentage from MD simulations and theoretical predictions of eqn (4).

Conflicts of interest

There are no conflicts of interest to declare.

Acknowledgements

This work was supported by the Research Grants Council of the Hong Kong Special Administrative Region (No. 16209119) and the Basic Science Center Program for Ordered Energy Conversion of the National Natural Science Foundation of China (No. 51888103).

References

1 Q. Wang and R. Li, *Renewable Sustainable Energy Rev.*, 2017, **74**, 715–720.
2 Y. Yang, L. Wang, Y. Fang and C. Mou, *Renewable Sustainable Energy Rev.*, 2017, **76**, 1465–1478.
3 M. Guo, X. Lu, C. P. Nielsen, M. B. McElroy, W. Shi, Y. Chen and Y. Xu, *Renewable Sustainable Energy Rev.*, 2016, **66**, 742–750.
4 V. Arora and Y. Cai, *Appl. Energy*, 2014, **120**, 95–103.
5 E. Krogulec and K. Sawicka, *Episodes*, 2015, **38**, 9–20.
6 A. Krupnick and H. Gordon, *Agricultural and Resource Economics Review*, 2015, **44**, 106–119.
7 A. Vengosh, R. B. Jackson, N. Warner, T. H. Darrah and A. Kondash, *Environ. Sci. Technol.*, 2014, **48**, 8334–8348.
8 J. D. Hughes, *Nature*, 2013, **494**, 307–308.
9 T. A. Ho, L. J. Criscenti and Y. Wang, *Sci. Rep.*, 2016, **6**, 28053.
10 W. Dang, J.-C. Zhang, X. Tang, X.-L. Wei, Z.-M. Li, C.-H. Wang, Q. Chen and C. Liu, *Geosci. Front.*, 2018, **9**, 559–575.
11 D. Dasani, Y. Wang, T. T. Tsotsis and K. Jessen, *Ind. Eng. Chem. Res.*, 2017, **56**, 9953–9963.
12 T. F. T. Rexer, M. J. Benham, A. C. Aplin and K. M. Thomas, *Energy Fuels*, 2013, **27**, 3099–3109.
13 G. P. Lithoxoos, A. Labropoulos, L. D. Peristeras, N. Kanellopoulos, J. Samios and I. G. Economou, *J. Supercrit. Fluids*, 2010, **55**, 510–523.
14 X. Zhu and Y.-P. Zhao, *J. Phys. Chem. C*, 2014, **118**, 17737–17744.
15 H. Wu, J. Chen and H. Liu, *J. Phys. Chem. C*, 2015, **119**, 13652–13657.
16 K. Bartus and A. Brodka, *Mol. Phys.*, 2011, **109**, 1691–1699.
17 S. J. Mahdizadeh and S. F. Tayyari, *Theor. Chem. Acc.*, 2011, **128**, 231–240.
18 L. Liu, C. Hu, D. Nicholson and S. K. Bhatia, *Langmuir*, 2017, **33**, 6280–6291.
19 L. Huang, L. Zhang, Q. Shao, L. Lu, X. Lu, S. Jiang and W. Shen, *J. Phys. Chem. C*, 2007, **111**, 11812–11920.
20 L. Lu, S. Wang, E. A. Muller, W. Cao, Y. Zhu, X. Lu and G. Jackson, *Fluid Phase Equilib.*, 2014, **362**, 227–234.
21 L. Liu, D. Nicholson and S. K. Bhatia, *Chem. Eng. Sci.*, 2015, **121**, 268–278.
22 W. Cao, L. Lu, M. Zhou, G. M. Tow, L. Huang, T. Yang and X. Lu, *Mol. Simul.*, 2017, **43**, 502–509.
23 L. Hong, D. Gao, J. Wang and D. Zheng, *AIP Adv.*, 2020, **10**, 015338.
24 H. Yu, J. Yuan, W. Guo, J. Cheng and Q. Hu, *Int. J. Coal Geol.*, 2008, **73**, 156–166.
25 S. Bhowmik and P. Dutta, *Energy Fuels*, 2011, **25**, 2730–2740.
26 P. Huo, D. Zhang, Z. Yang, W. Li, J. Zhang and S. Jia, *Int. J. Greenhouse Gas Control*, 2017, **66**, 48–59.
27 J. Shi, L. Gong, S. Sun, Z. Huang, B. Ding and J. Yao, *RSC Adv.*, 2019, **9**, 25326–25335.
28 H. Zhang and D. Cao, *Chem. Eng. Sci.*, 2016, **156**, 121–127.
29 H. Sun, H. Zhao, N. Qi and Y. Li, *J. Phys. Chem. C*, 2017, **121**, 10233–10241.
30 T. A. Ho, Y. Wang, Y. Xiong and L. J. Criscenti, *Fuel*, 2018, **220**, 1–7.
31 Q. Yuan, X. Zhu, K. Lin and Y.-P. Zhao, *Phys. Chem. Chem. Phys.*, 2015, **17**, 31887–31893.
32 Y. Yang, A. K. N. Nair and S. Sun, *J. Phys. Chem. C*, 2020, **124**, 16478–16487.
33 P. Li, Z. Jiang, M. Zheng, H. Bi and L. Chen, *J. Nat. Gas Sci. Eng.*, 2016, **34**, 1034–1043.
34 K. Ji, S. Guo and B. Hou, *J. Pet. Sci. Eng.*, 2017, **150**, 250–256.
35 C. Zou, Q. Zhao, D. Dong, Z. Yang, Z. Qiu, F. Liang, N. Wang, Y. Huang, A. Duan, Q. Zhang and Z. Hu, *J. Nat. Gas Geosci.*, 2017, **2**, 273–288.
36 H. Berendsen, J. P. M. Postma, W. van Gunsteren, A. D. DiNola and J. R. Haak, *J. Chem. Phys.*, 1984, **81**, 3684–3690.
37 M. Parrinello and A. Rahman, *J. Appl. Phys.*, 1981, **52**, 7182–7190.
38 U. Setzmann and W. Wagner, *J. Phys. Chem. Ref. Data*, 1991, **20**, 1061–1155.
39 R. Span and W. Wagner, *J. Phys. Chem. Ref. Data*, 1996, **25**, 1509–1596.
40 S. L. Mayo, B. D. Olafson and W. A. Goddard, *J. Phys. Chem.*, 1990, **94**, 8897–8909.
41 J. Gasteiger and M. Marsili, *Tetrahedron*, 1980, **36**, 3219–3228.
42 J. Xiong, K. Liu, L. Liang and Q. Zeng, *RSC Adv.*, 2016, **16**, 110808–110819.
43 R. L. June, A. T. Bell and D. N. Theodorou, *J. Phys. Chem.*, 1990, **94**, 8232–8240.
44 Q. Yang and C. Zhong, *J. Phys. Chem. B*, 2006, **110**, 17776–17783.
45 T. F. Rexer, E. J. Mathia, A. C. Aplin and K. M. Thomas, *Energy Fuels*, 2014, **28**, 2886–2901.
46 X. Cheng, Z. Li and Y.-L. He, *RSC Adv.*, 2020, **10**, 37507–37514.
47 X. Cheng, Z. Li and Y.-L. He, *RSC Adv.*, 2019, **9**, 9546–9554.